

Direct numerical simulation of heat transfer from the stagnation region of a heated cylinder affected by an impinging wake

JAN G. WISSINK¹† AND WOLFGANG RODI²

¹School of Engineering and Design, Brunel University, Kingston Lane, Uxbridge, UB8 3PH, UK

²Institute for Hydromechanics, Karlsruhe Institute of Technology, Kaiserstr. 12, D-76128 Karlsruhe, Germany

(Received 3 September 2009; revised 16 September 2010; accepted 16 September 2010;
first published online 14 January 2011)

The effect of an incoming wake on the flow around and heat transfer from the stagnation region of a circular cylinder was studied using direct numerical simulations (DNSs). Four simulations were carried out at a Reynolds number (based on free-stream velocity and cylinder diameter D) of $Re_D = 13\,200$: one two-dimensional (baseline) simulation and three three-dimensional simulations. The three-dimensional simulations comprised a baseline simulation with a uniform incoming velocity field, a simulation in which realistic wake data – generated in a separate precursor DNS – were introduced at the inflow plane and, finally, a simulation in which the turbulent fluctuations were removed from the incoming wake in order to study the effect of the mean velocity deficit on the heat transfer in the stagnation region. In the simulation with realistic wake data, the incoming wake still exhibited the characteristic meandering behaviour of a near-wake. When approaching the regions immediately above and below the stagnation line of the cylinder, the vortical structures from the wake were found to be significantly stretched by the strongly accelerating wall-parallel (circumferential) flow into elongated vortex tubes that became increasingly aligned with the direction of flow. As the elongated streamwise vortical structures impinge on the stagnation region, on one side they transport cool fluid towards the heated cylinder, while on the other side hot fluid is transported away from the cylinder towards the free stream, thereby increasing the heat transfer. The DNS results are compared with various semi-empirical correlations for predicting the augmentation of heat transfer due to free-stream turbulence.

Key words: buoyant boundary layers, turbulence simulation, vortex interactions

1. Introduction

Turbine blades are exposed to fairly strong free-stream turbulence, both uniformly distributed turbulence originating partly from the combustion chamber and turbulence concentrated in periodically passing wakes generated by the preceding row of blades. The impinging free-stream turbulence is known to increase significantly the heat transfer to the blades and hence their heat load. Profound knowledge about this effect and the ability to predict it are of great importance for the design of

† Email address for correspondence: jan.wissink@brunel.ac.uk

efficient turbine-blade cooling systems. Free-stream turbulence usually causes earlier transition of the boundary layer on the suction surface of turbine blades, which is accompanied by an increase in heat transfer due to the turbulent fluctuations in the boundary layer beyond transition. However, an increase in heat transfer due to free-stream turbulence was also found in regions in which the boundary layer remains laminar, such as in pre-transitional regions on the suction surface, often on the entire pressure side and especially in the leading-edge stagnation-flow region. This important phenomenon is the subject of this paper, and following Dullenkopf & Mayle (1994, 1995), we call this an increase of ‘laminar’ heat transfer, as the boundary layer is hydrodynamically laminar in the situations considered. The phenomenon can also be found in the front region of flow around a circular cylinder so that this configuration has often been used to study the effect of free-stream turbulence on laminar heat transfer.

The influence of free-stream turbulence on laminar heat transfer has been studied experimentally for various configurations. In their experiments on laminar heat transfer along a flat plate affected by free-stream fluctuations, Kestin, Maeder & Wang (1961) and Junkhan & Serovy (1967) discovered that in order for these fluctuations to be able to increase heat transfer rates, the affected laminar-boundary-layer flow needs to be accelerating. This finding was confirmed by the experiments of Schulz (1986), who measured the heat transfer distributions around a typical fore-loaded aerofoil for several free-stream turbulence levels. Strong acceleration is present in the stagnation region of a circular cylinder, and heat transfer experiments for this situation as well as for aerofoils available in the early 1990s have been reviewed by Dullenkopf & Mayle (1994). These authors then used the results to develop a correlation for the increase in heat transfer, with the turbulence level Tu , the Reynolds number Re_D and the free-stream acceleration (strain rate a) as parameters. This correlation represents the data quite well for both cylinder and aerofoil configurations where the acceleration is constant, but there is relatively large scatter at medium free-stream turbulence levels. In a follow-up paper, Dullenkopf & Mayle (1995) attributed this to the influence of the length scale L of the impinging turbulence and introduced L into a new correlation which shows less scatter. According to this correlation, for small length scales the heat transfer increases first with growing L and then reaches a maximum, and at larger length scales it decreases with further increasing L so that there the heat transfer augmentation is proportional to $Tu/L^{1/3}$. On the basis of rapid distortion theory, Ames & Moffat (1990) arrived at the same dependence, and in both correlations the augmentation is in addition roughly proportional to the square root of the Reynolds number. Ames, Wang & Barbot (2003) studied experimentally the heat transfer augmentation in the stagnation region of a vane for various levels of inlet turbulence intensity and scale as well as Reynolds number. They found that the Ames–Moffat correlation describes their results fairly well. Van Fossen, Simoneau & Ching (1995) conducted a series of stagnation-region heat transfer measurements on elliptical leading-edge models for various levels of Reynolds number and grid-generated turbulence intensities and scales. They found a similar dependence of heat transfer augmentation on these parameters, albeit represented by a somewhat different correlation than mentioned above.

In the studies discussed so far, the approach flow carried grid-type turbulence; i.e. it was approximately homogeneous and isotropic. Dullenkopf, Schulz & Wittig (1991) and Liu & Rodi (1994*a, b*) performed heat transfer measurements of flow over turbine blades with incoming wakes, i.e. where the free-stream turbulence was concentrated in periodically passing wakes. They found that in the accelerating laminar flow regions

on both the suction and pressure sides the heat transfer increased significantly with increasing wake frequency.

From the above experiments, the following conclusions related to the augmentation of laminar heat transfer due to free-stream turbulence may be drawn.

(i) For free-stream turbulence to be able to increase laminar heat transfer, the boundary-layer flow needs to be accelerating.

(ii) The augmentation of laminar heat transfer increases with increasing Reynolds number and turbulence level and with decreasing length scales.

(iii) With increasing wake frequency, periodically impinging wakes were found to increase the heat transfer along turbine blades at low Reynolds numbers.

1.1. *The turbulence that matters*

The experimental data of Sikmanovic, Oka & Koncar-Djurdjevic (1974), Lowery & Vachon (1975), Van Dresar (1987), van Fossen *et al.* (1995), Ames & Moffat (1990) and Ames *et al.* (2003) have shown that the effect of turbulence and heat transfer generally decreases with an increase in turbulence length scale. Examining the length-scale influence in more detail, Yardi & Sukhatme (1978) found in their experiments that the augmentation of heat transfer in the stagnation region of a cylinder is largest when the integral length scale Λ of the approach-flow turbulence is between 4 and 12 times the boundary-layer thickness δ , reducing sharply for smaller scales and more slowly when the scale is increased beyond this range. A similar behaviour was derived by Xiong & Lele (2004) by way of a theoretical analysis of the distortion of two-dimensional stagnation-point flow by three-dimensional disturbances. From this analysis the authors found that the disturbance most effective for increasing heat transfer had a length scale close to 5 times the boundary-layer thickness δ .

Dullenkopf & Mayle (1995) focused on the question of how free-stream turbulence affects laminar heat transfer. The concepts of an ‘effective’ frequency (or length scale) and an ‘effective’ turbulence level were developed in their study of the increase of laminar heat transfer owing to a turbulent approach flow. Free-stream fluctuations with an integral length scale Λ such that $\Lambda/\delta \approx 9$ were found to cause the most significant increase in laminar heat transfer. This is in line with the earlier finding of Yardi & Sukhatme (1978) who determined the maximum effect to be at $\Lambda/\delta \approx 10$. Hence, only a selected band of wavenumbers in the energy-containing range of the free-stream turbulence spectrum was found to be able to cause a significant increase in laminar heat transfer.

In the paper of Mayle, Dullenkopf & Schulz (1998), entitled ‘The turbulence that matters’, the role of free-stream turbulence was examined further, and a more coherent picture of its effects on laminar heat transfer was presented. A unified expression for the one-dimensional spectrum of turbulence was obtained, which properly accounts for all scales of turbulence and allows one to relate the ‘heat-transfer-effective’ turbulence levels and frequencies to a Reynolds number of the free-stream fluctuations involving their length scale.

1.2. *Physical mechanisms*

Hunt (1973) used rapid distortion theory to predict the response of small- and large-scale turbulent eddies to the straining experienced in the stagnation region of a cylinder. His results were later corroborated by the cylinder experiments of Britter, Hunt & Mumford (1979). These studies determined that eddies which are relatively small compared with the cylinder radius are amplified in their fluctuations as they are stretched and rotated by the accelerating mean flow. This effect is felt in a region

up to about three radii from the cylinder wall. A second effect is the blocking of the eddies by the cylinder surface, which is associated with the splatting effect. This is felt up to one integral length from the wall and is the dominant effect for relatively large eddies. As was mentioned earlier, the disturbance amplification predicted by Hunt's theory was the basis for the heat transfer correlation developed by Ames & Moffat (1990). The phenomena described here take place outside the very thin boundary layer on the cylinder. Another theoretical study including the boundary layer was conducted by Xiong & Lele (2004) who presented an analysis of the distortion of unsteady three-dimensional disturbances in a Hiemenz boundary layer (stagnation flow on a plane surface) and the associated enhancement of heat transfer. For certain disturbance length scales (especially $\Lambda/\delta \approx 5$) a large amplification of vorticity was obtained with strong vortices developing close and parallel to the wall. With their motion towards the wall on one side and away from the wall on the other side, these vortices are the primary cause of the heat transfer augmentation. On the basis of their analysis, Xiong & Lele (2004) developed a scaling correlation for stagnation-point heat transfer which has a similar parameter dependence as the one of Ames & Moffat (1990) but lacks a quantitative coefficient.

From the above studies it can already be concluded that the main mechanism responsible for the increase in heat transfer due to free-stream turbulence is its stretching, causing strong vortices aligned along the wall which exchange heat normal to the wall – and this explains why the augmentation is found only in accelerating flow. The augmented turbulence interacts with the boundary layer, but in the stagnation regions, and on turbine blades also in other regions with strong acceleration, this remains laminar in the mean, even though the flow is instantaneously very unsteady and irregular (Paxson & Mayle 1991). The phenomenon of shear sheltering limits the penetration of free-stream vortical structures into the boundary layer. This mechanism is mainly effective for small scales, while the larger scales are much less sheltered and manage to penetrate deeper and more easily into the boundary layer (Hernon, Walsh & McEligot 2007). Disturbances that penetrate into the boundary layer will have an impact on the heat transfer, and as the small disturbances are sheltered, it is the larger-scale structures of the size 5–10 times the boundary-layer thickness that are the most effective in increasing laminar heat transfer. However, one cannot really speak of penetration any longer because such large eddies instantaneously disturb strongly or even destroy the boundary layer. When the eddies are very large compared with the boundary-layer thickness, the disturbance is quasi-steady, which explains the diminishing augmentation effect with increasing length scale. However, the precise way in which free-stream vortical structures manage to increase the heat transfer still needs further clarification. To this end, detailed studies of these effects through direct numerical simulations (DNSs) and large-eddy simulations (LESs) of boundary-layer flow with free-stream disturbances and passive heat transfer would be very helpful.

The first DNSs of heat transfer from a heated turbine-blade model exposed to oncoming wakes and free-stream fluctuations were performed by Wissink & Rodi (2006). The set-up of the problem was in accordance with the experiments performed by Liu & Rodi (1994*a,b*). It was found that the presence of wakes and free-stream fluctuations does promote the heat transfer along the pressure side, where the boundary layer remains laminar at all times, and also along the suction side including the pre-transitional laminar part. In both regions with laminar boundary layer the flow accelerates, thereby stretching the vortices of the free-stream turbulence, aligning their axes with the flow direction and forming streamwise vortical structures.

These increase the heat transfer through an upwash of hot fluid towards the free stream and a downwash of ambient cold fluid towards the blade. In a later DNS of the accelerating flow over and laminar heat transfer from a flat plate under the influence of grid turbulence in the free stream, Wissink & Rodi (2009) observed the same mechanism responsible for causing an increase in heat transfer. An LES study of stagnation-point flow and heat transfer under free-stream turbulence was performed by Xiong & Lele (2007). Also in this case, intense quasi-streamwise vortices were observed to develop owing to the strong vortex stretching near the leading edge, and these were found to be the direct cause of the heat transfer enhancement predicted. Very recently, Bhaskaran & Lele (2010) performed an LES study of free-stream turbulence effects on heat transfer to a high-pressure turbine cascade. This study revealed the presence of streamwise streaky structures along both the suction and pressure sides that appeared to be initiated by longitudinal vortical structures that form as vortices are stretched around the leading edge. The streaky structures were found to cause a significant enhancement of blade heat transfer.

1.3. Present contribution

The present paper reports on DNSs of heat transfer from the stagnation region of a circular cylinder in the presence of an oncoming wake. This allows the study, under simplified conditions, of the mechanisms governing the heat load of turbine blades subjected to impinging turbulent wakes. The set-up of the numerical simulation was inspired by the experiments of Magari & LaGraff (1994), who used a small cylinder (diameter $D/4$) located $2D$ upstream of a larger heated cylinder with diameter D to study the wake-induced increase in heat transfer in the stagnation region of the large cylinder. The present numerical study aims to shed further light on the physical mechanisms that play a role in this wake-induced increase in laminar heat transfer. To achieve this, a good understanding of the deformation of vortical structures from the incoming wake by the strongly accelerating flow near the stagnation region of the cylinder is of paramount importance. The experimental situation of Magari & LaGraff (1994) could not be simulated directly by DNSs because of the relatively large Reynolds number ($Re_D = (U_0 D)/\nu = 48\,000$) and the relatively small distance between the two cylinders, which would have required the joint resolution of the flow around both cylinders. Rather, wake data readily available from a previously performed precursor DNS of the flow around a single cylinder at a relatively low Reynolds number (Wissink & Rodi 2008) were prescribed as inflow conditions for the DNS of flow around the heated larger cylinder. This allows a high resolution and a high-quality mesh for this simulation.

As the curvature of the stagnation area of a circular cylinder and that of the leading edge of many turbine blades are identical, the results in the present simulation are immediately transferable to blade geometries. Another advantage of the configuration studied is the possibility of comparing the predicted influence of the free-stream turbulence on the stagnation heat transfer directly with the various experimental correlation curves mentioned above.

2. Computational details

2.1. Computational method

The simulations were performed employing a second-order accurate central finite-volume discretisation in space of both the incompressible, three-dimensional Navier–Stokes equations and the convection–diffusion equation for the temperature T , using

Simulation	Wake		Tu ($y/D=0$) (%)	l_z
	Half-width	Velocity deficit (%)		
A	–	–	0.0	$2D$
A.2	–	–	0.0	$0.02D$
B	$0.152D$	25	25.5	$2D$
C	$0.152D$	25	0.0	$2D$

TABLE 1. Overview of the DNSs performed. In all simulations 411 points are employed in the radial direction. In simulations A, B and C, 1606 points are employed in the circumferential direction, while in simulation A.2, 806 points are employed to cover the modelled half of the circumference of the cylinder. In the spanwise direction of the three-dimensional simulations A, B and C, 512 grids are used, while in the effectively two-dimensional simulation A.2, 4 grid points are employed. The wake's half-width, velocity deficit and Tu -level (at its axis) are given at the inlet plane of the computational domain.

a collocated variable arrangement. The Prandtl number adopted in the calculation of T was $Pr = 0.71$. To avoid a decoupling of the velocity and pressure fields, the momentum interpolation procedure of Rhie & Chow (1983) has been applied. The code has been parallelised using the standard Message-Passing Interface protocol. To achieve a near-optimal load balancing, the computational grid has been subdivided into blocks of equal size, each of which has been assigned to its own unique processor. Time integration has been performed using a three-stage Runge–Kutta method. More information on the basic numerical code can be found in Breuer & Rodi (1996).

The four simulations that were performed are itemised in table 1, where the turbulence level Tu is defined as

$$Tu = \sqrt{\frac{(u'u' + v'v' + w'w')/3}{U_0^2}} \times 100 \%. \quad (2.1)$$

2.2. Computational domain and boundary conditions

A spanwise cross-section of the computational domain used in simulations A, B and C (see table 1) is displayed in figure 1. The inflow plane is located at $x/D = -5.0$, and the outflow plane is at $x/D = 10.0$. In simulations B and C, at the inflow plane, wake data (u_w, v_w, w_w) were superposed on the mean field $(u, v, w) = U(1, 0, 0)$, giving

$$(u_{in}, v_{in}, w_{in}) = U(1, 0, 0) + (u_w, v_w, w_w). \quad (2.2)$$

The wake data used in simulation B were generated in a precursor DNS (Wissink & Rodi 2008) of the flow around a circular cylinder at $Re_d = 3300$ – based on the inflow velocity U_0 and the diameter of the small cylinder $d = D/4$ – and consist of a series of snapshots of the instantaneous velocity in the vertical plane located at a distance of $6d$ downstream of the centre of the cylinder. More information on the preparation of the wake data can be found in Zaki *et al.* (2009). Since the diameter of the small cylinder is $d = D/4$, the Reynolds number Re_D based on D is $Re_D = 13\,200$. It should be noted that, along the wake axis, the distance from the centre of the small cylinder to the inflow plane is $6d = 1.5D$, and the distance to the stagnation line of the large cylinder – at $((x/D, y/D) = (-0.5, 0.0))$ – is $24d = 6D$. At a distance of $24d$ downstream of the small cylinder, the wake impinging on the large cylinder still shows significant traces of the individual vortices that were shed alternately from the upper and lower sides of the small cylinder. In simulation C the temporal fluctuations

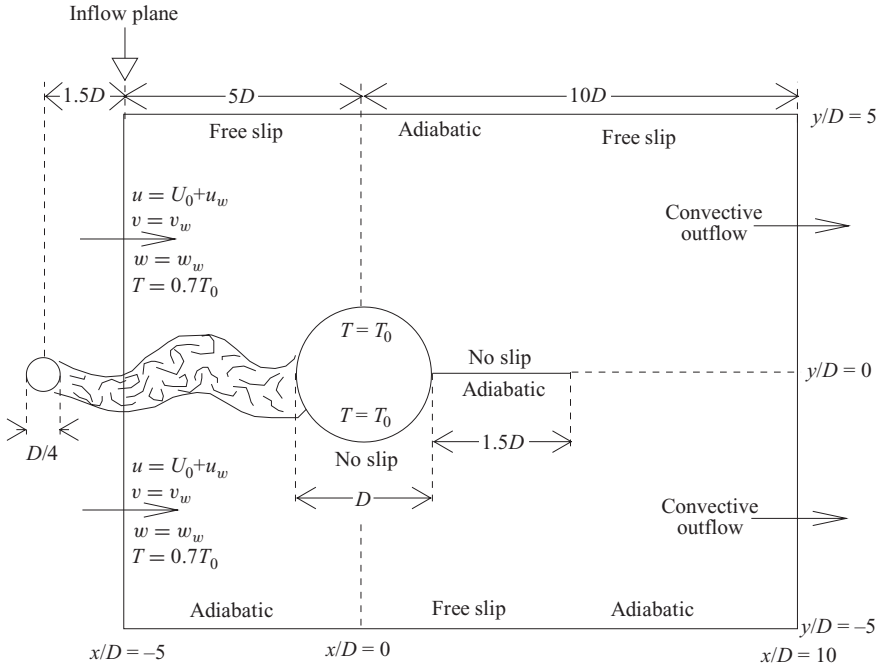


FIGURE 1. Schematic of the computational domain.

were removed from the wake, thereby effectively replacing it by a negative jet with a velocity profile (at the inflow plane) that is identical to that of the time-averaged wake used in simulation B. Similar to the experiment of Magari & LaGraff (1994), the formation of a vortex street behind the cylinder – which may introduce oscillations in the location of the stagnation line – is suppressed by introducing a thin splitter plate along the horizontal axis of the computational domain between $x/D = 0.5$ and $x/D = 2.0$. At the surface of the splitter plate, no-slip boundary conditions were prescribed for the velocity, and adiabatic conditions were applied for the temperature. At the upper and lower boundaries of the calculation domain ($y/D = \pm 5D$), free-slip boundary conditions were employed for the velocity, and adiabatic conditions were applied for the temperature. On the surface of the cylinder, no-slip boundary conditions and a constant temperature $T = T_0$ were prescribed. The temperature of the incoming flow was chosen to be constant, $T = 0.7T_0$. At the outflow plane a convective boundary condition was prescribed. The size of the spanwise extent of the computational domain was chosen as $l_z = 2D$, and periodic conditions were employed at the boundaries. As we are interested only in the stagnation-region flow and not in the flow behind the large cylinder, this spanwise size – that was based on the actual size of $8d$ used in the precursor simulation – is deemed to be large enough to accommodate even the largest spanwise modes present in the incoming wake.

In both simulations A and A.2, a uniform flow field was employed at the inflow plane. Compared with simulation A, simulation A.2 has a reduced spanwise size of only $l_z = 0.02D$ and is, hence, effectively two-dimensional. Also, in simulation A.2 only the upper half of the computational domain is computed, and a symmetry condition is used to model the lower half. By following this strategy all wall-parallel fluctuations of the stagnation-region flow (for instance due to the vortex shedding downstream) are eliminated.

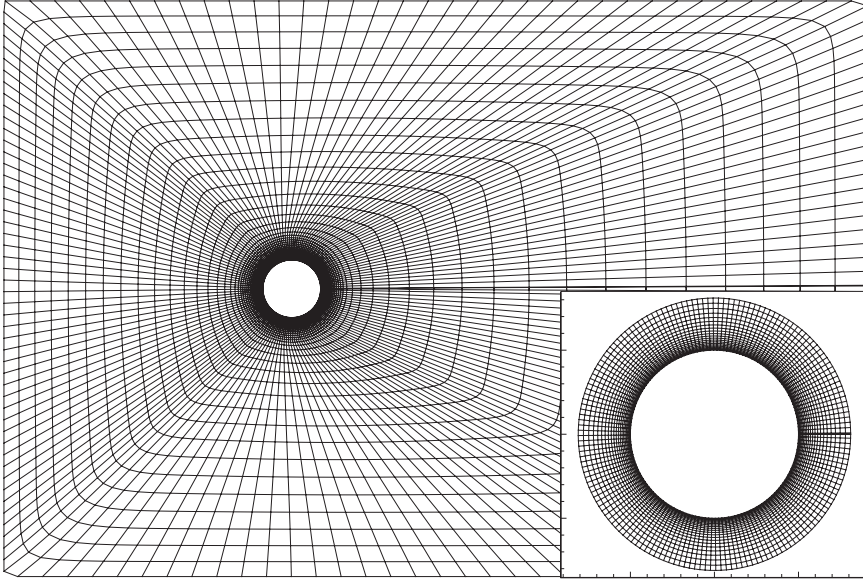


FIGURE 2. Computational mesh showing every 10th grid line in the (x, y) -plane.

2.3. Computational mesh

The computational mesh at the midspan is illustrated in figure 2, showing every 10th grid line. The O-mesh provides a good resolution of the flow upstream and in the immediate vicinity of the cylinder. The calculations were performed on the Altix cluster of the Leibniz Computing Centre in Munich, using 338 million grid points and 480 processors. The time step employed in the simulations was $\delta t \approx 2 \times 10^{-4} L/U$. For each simulation approximately 150 000 time steps were required to complete it. As a result, each simulation took slightly more than a month (823 clock hours) of continuous running to finalise. The meshes used in the present simulations were designed using our experience gained in the elaborate grid refinement study reported in Wissink & Rodi (2008). Figure 3 shows the grid resolution in wall units along the upper side of the cylinder. It illustrates that the boundary layer is well resolved. The distance between the wall and the wall-nearest grid point, Δy^+ , was always less than 0.3 wall units, indicating that the viscous sublayer was well resolved. Adjacent to the cylinder, the point-to-point distances in the streamwise and spanwise directions were $\Delta x^+ < 4$ and $\Delta z^+ < 7$ wall units, respectively.

3. Results

3.1. Flow characteristics

3.1.1. Time-averaged statistics of the flow field

The predicted characteristics of the approach flow are presented first. In figure 4 the profiles of the time-averaged velocity in the x -direction in the inflow region are compared at $x/D = -5, -4, \dots, -1$. It can be seen that at the inflow plane at $x/D = -0.5$ the profiles of simulations B and C exactly match, while the profile of simulation A is uniform. Downstream of the inflow plane, the U -velocity profile of simulation A starts to develop an increasing velocity deficit which is entirely caused by the upstream effect of the cylinder. Although at $x/D = -1$ the velocity

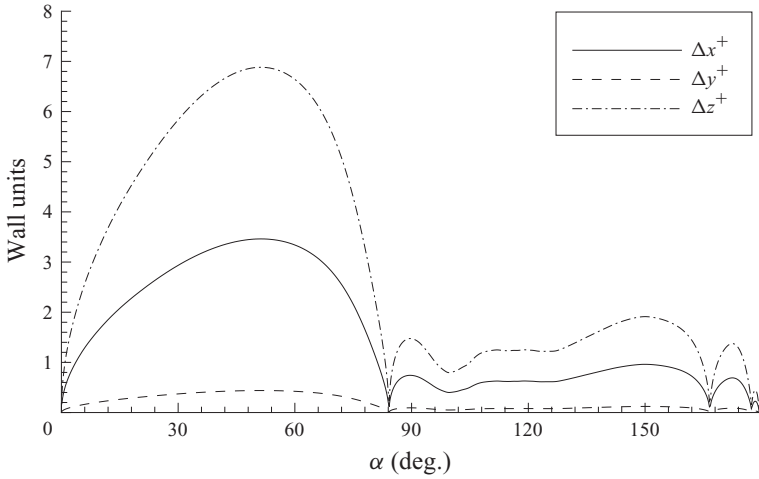


FIGURE 3. Distances between wall-adjacent points in wall units along the cylinder from simulation B: x^+ and z^+ , wall-parallel point-to-point; y^+ , wall-adjacent point to the surface.

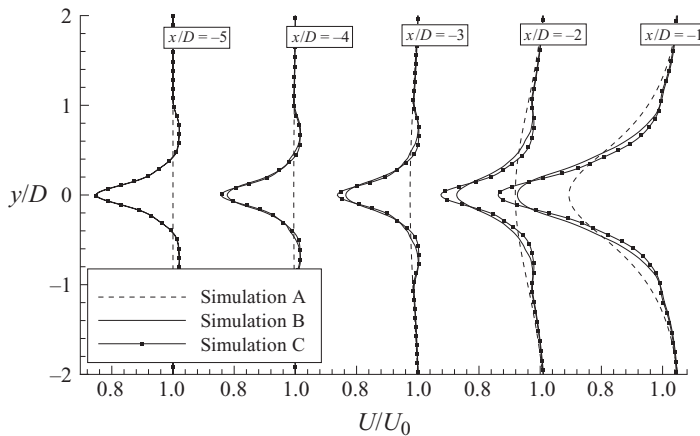


FIGURE 4. Simulations A, B and C: inflow profiles and their development in the midplane.

deficit in simulation A has become quite large, it still is significantly less than the deficits in simulations B and C that also tend to grow because of stagnation effects when approaching the cylinder. Compared with simulation C, the velocity deficit in simulation B can be seen to become increasingly smaller, which is explained by the presence of turbulent shear stress in this case.

Figure 5(a) shows the development of the root-mean-square values of u' , v' and w' fluctuations from simulation B – made dimensionless by U_0 – along the $y/D = 0$ axis. Initially, the v' fluctuations in the vertical direction are significantly larger than the fluctuations in the other directions, which reflects the large-scale vertical oscillation in the incoming wake related to the vortex shedding. Farther downstream this oscillation is significantly damped, and the incoming turbulence appears to become virtually isotropic at $x/D \approx -0.7$. While v' is reduced significantly, u' and w' only decline very gradually. Very near to the cylinder the fluctuations increase again because of the straining discussed earlier, and the spanwise fluctuation becomes largest because of the splatting effect. A similar behaviour was also found in the LES of Xiong &

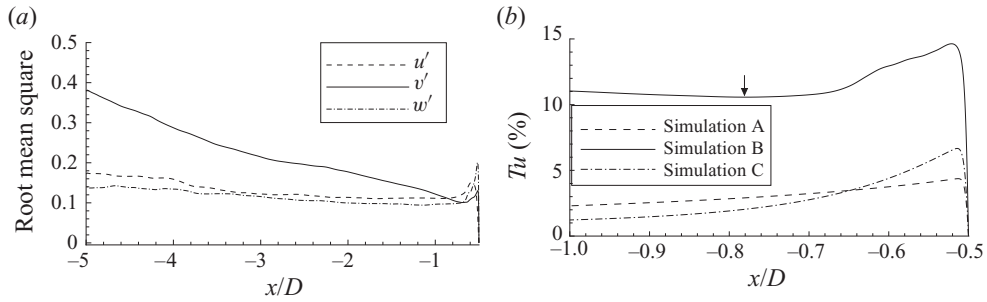


FIGURE 5. Profiles in the approach-flow area at $y/D=0$. (a) Root-mean-square profiles of u' , v' and w' from simulation B and (b) Tu from simulations A, B and C.

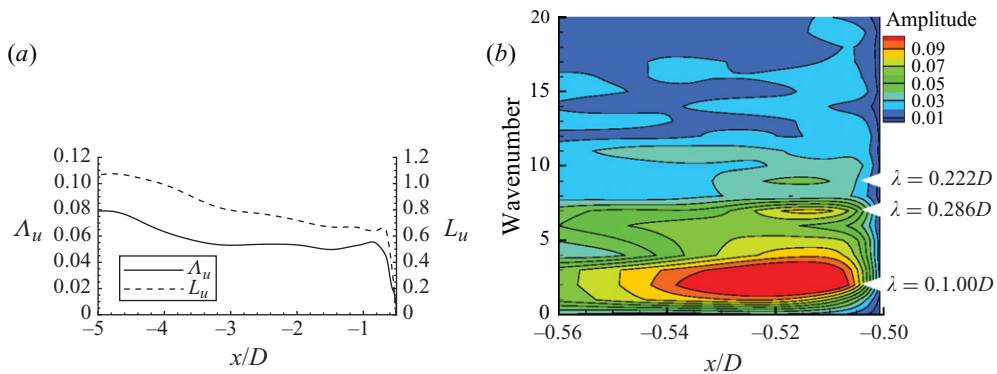


FIGURE 6. Simulation B: (a) variation of the spanwise integral length scale Λ_u and energy scale L_u in the approach flow along $y/D=0$; (b) contour plot representing the time-averaged amplitude of the modes in one-dimensional spanwise spectra of the w -velocity along $y/D=0$, immediately upstream of stagnation.

Lele (2007). Figure 5(b) displays the corresponding behaviour of the turbulence level Tu defined in (2.1) which, of course, also increases near the stagnation point. The figure shows that even in the absence of incoming fluctuations (simulations A and C) low-level fluctuations caused by some vortex shedding behind the cylinder are present in front of the cylinder. Consequently, the presence of the splitter plate is clearly not sufficient to completely avoid oscillations in this region.

Figure 6(a) shows the evolution of the spanwise integral length scale Λ_u based on the u -velocity and the energy length scale $L_u = 1.5|u'|^3/\varepsilon$, where ε is the turbulence dissipation rate, which is calculated via its definition from the gradients of the velocity fluctuations; L_u is determined by the size of energy-rich scales and is an order of magnitude larger than Λ_u , but both length scales have a similar development, first decreasing gradually and then dropping to zero when the stagnation line is approached. The integral length scale Λ_u is of the order of 5–7 times the boundary-layer thickness ($\delta \lesssim 0.01D$; see figures 8 and 21) so that according to the findings reported in § 1.2 it is in the effective range for increasing the heat transfer.

Figure 6(b) shows a carpet plot of spanwise spectra of the instantaneous w -velocity along $y/D=0$ in the near-stagnation region. Moving towards the location of stagnation, at $x/D = -0.5$, the amplitudes of several modes can first be seen to increase and then subsequently quickly decrease when the wall is approached. The

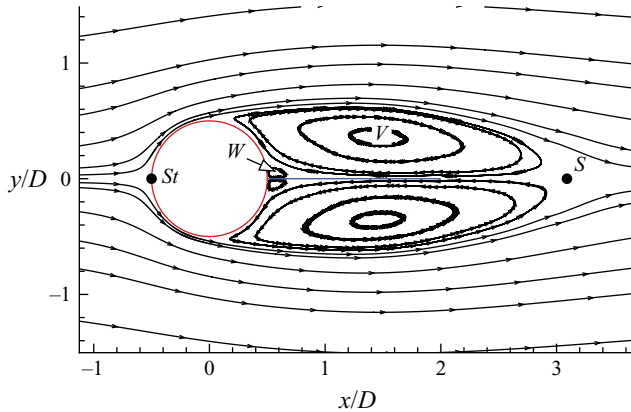


FIGURE 7. (Colour online) Simulations B: time-averaged streamlines at the midspan.

observed increase in the amplitude of the smaller modes (larger wavenumbers such as $k = 7, 9$) corroborates the theoretical results of Hunt (1973), according to which these modes are amplified by the mean field straining. However, the amplitude of the modes with wavenumbers $k = 2, 3$ can also be seen to grow significantly. These modes represent fairly large eddies that contain most of the energy and are the main contributor to the root-mean-square value of w' . Their amplification is caused by the transfer of energy from the streamwise to the spanwise fluctuations due to the splatting effect, as can be seen also from the near-wall behaviour of u' and w' in figure 5(a). It should be noted that the mode with wavenumber $k = 7$ has a wavelength of $\lambda = 0.286D$, which is close to the diameter of approximately $0.25D$ of the vortices with streamwise rotation in the incoming wake (Wissink & Rodi 2008). This also corresponds roughly to the distance between the high- w' -fluctuation patches (figure 11) and high-temperature streaks (figures 19b, 21 and 22).

Turning now to the flow around and past the cylinder, figure 7 shows the time-averaged streamlines at the midspan of simulation B. The location of the stagnation line is identified by St ; the location of the downstream saddle point $(x/D, y/D) = (0.309, 0.0)$, which corresponds to the end of separation, is identified by S ; the centre of the main recirculation region above the splitter plate is identified by V ; and finally, the small vortex observed in the corner of the splitter plate and the back wall of the cylinder is identified by W . The two major recirculation regions can be seen to extend beyond the trailing edge (located at $x/D = 2$) of the splitter plate.

Figure 8 compares profiles of the boundary layers from simulations A, B and C at various stations ($\alpha = 10^\circ, 20^\circ, \dots, 50^\circ$) along the upper half of the cylinder, with $\alpha = 0^\circ$ identifying the stagnation line and $\alpha = 90^\circ$ the apex, where $(x/D, y/D) = (0, 0.5)$. Because of symmetry, the time-averaged circumferential velocity at the stagnation line has to be zero. Downstream of this location, the free-stream circumferential velocity can be seen to gradually increase. Because of the larger approach-flow velocity immediately in front of the cylinder in case A (see figure 4), the circumferential free-stream velocity is larger than in cases B and C. The close agreement between the boundary-layer profiles of cases B and C indicates that – despite the incoming fluctuations – the boundary layer in simulation B remains laminar. This is to be expected, as upstream of $\alpha = 60^\circ$ the acceleration parameter $K = (U_0 D / Re_D U^2) (\partial U_c / \partial \xi)$ (where U_c is the circumferential velocity and ξ the circumferential coordinate) assumes values well in excess of $K = 2.5 \times 10^{-6}$,

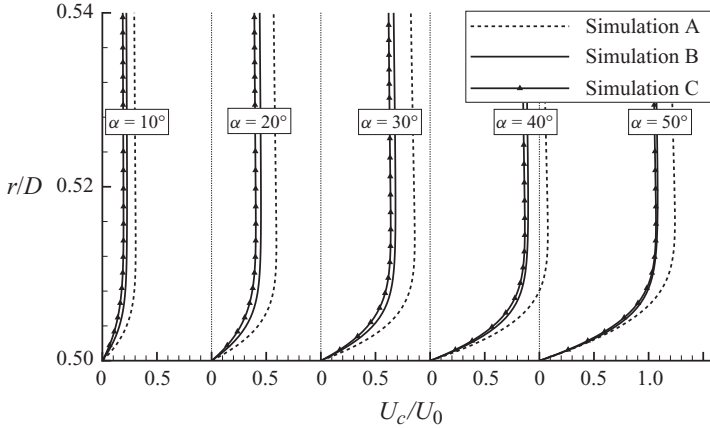


FIGURE 8. Simulations A, B and C: profiles of the streamwise (circumferential) velocity U_c in the boundary layer at $\alpha = 10^\circ, 20^\circ, \dots, 50^\circ$.

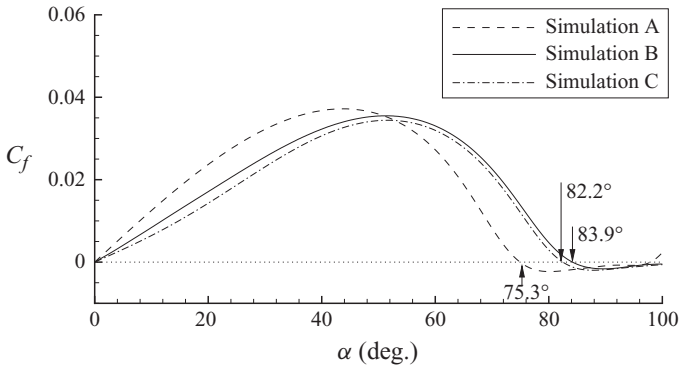


FIGURE 9. Simulations A, B and C: comparison of friction coefficient distribution along the front part of the cylinder. The arrows indicate the lines of separation.

which – according to the criterion of Jones & Launder (1973) – is sufficient to ensure that a laminar-boundary-layer flow will not undergo transition.

Again, because of the larger approach-flow velocity, the growth of the friction coefficient $C_f = (v(\partial U_c / \partial r)|_{wall}) / U_0^2$ (where r is the radial coordinate) downstream of the stagnation line – shown in figure 9 – is significantly larger in simulation A than in simulations B and C, which do not differ much. In simulations B and C, separation is located at $\alpha = 83.9^\circ$ and 82.2° , respectively. The slightly later separation observed in simulation B is likely to be caused by the boundary layer being energised by the impinging wake. The relatively early separation at $\alpha = 75.3^\circ$ observed in simulation A is mainly due to the different mean inflow profile. Note that for this type of flow (in the subcritical regime) transition takes place in the two separated shear layers somewhere downstream of the large cylinder.

Figure 10 shows a comparison of the total shear stress $s = (1/Re)|\partial(U_c/U_0)/\partial(r/D)| + \overline{u'_c u'_r} / U_0^2$ in simulations A, B and C and the fluctuation-induced shear stress $\overline{u'_c u'_r} / U_0^2$ in simulation B along the front part of the cylinder, where u_c and u_r are the velocity components in the circumferential and radial directions, respectively. In the stagnation region, close to the cylinder's surface, the total shear stress from simulation A is larger than the shear stress in simulations B and C, as was to be

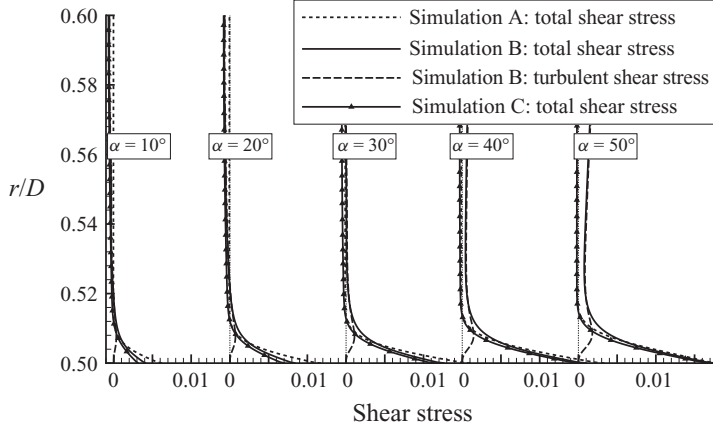


FIGURE 10. Simulations A, B and C: total and fluctuation-induced shear stresses.

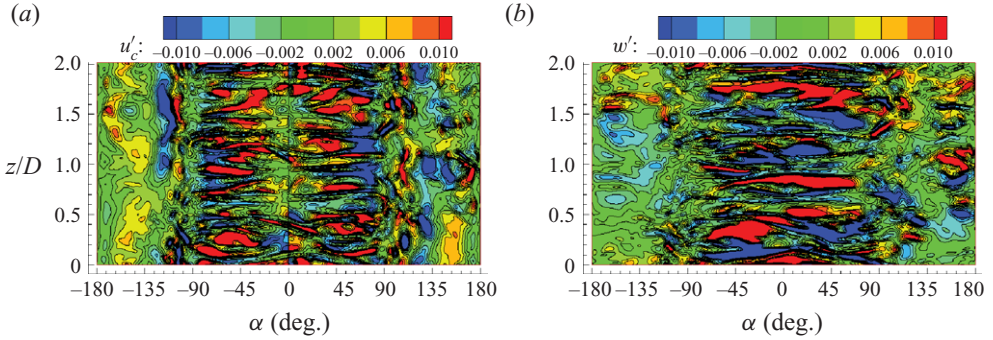


FIGURE 11. Simulation B: snapshots showing contours of the (a) streamwise and (b) spanwise wall-tangential velocity fluctuations in the grid plane at a distance of $0.00025D$ to the cylinder wall.

expected from figure 9. Farther away this difference gradually disappears. The total shear stress in simulations B and C is found to be quite similar close to the cylinder, while farther upstream the observed deviations can be attributed to the fluctuation-induced shear stress in simulation B, which in the near-wall region is, however, small compared with the viscous stress. This underlines the observation that the boundary layer remains laminar.

3.1.2. Instantaneous flow patterns

Figure 11 shows snapshots of the (a) streamwise and (b) spanwise fluctuating velocities from simulation B in the grid plane adjacent to the cylinder wall. The fluctuations in the streamwise velocity show the presence of streak-like elongated areas of high- and low-speed flow that appear in the developing boundary layers along both the upper and lower sides of the cylinder. In the immediate vicinity of the stagnation line, between $\alpha \approx -15^\circ$ and $\alpha \approx 15^\circ$, the streamwise fluctuations tend to be almost negligible, which is due to the splatting effect. The contours of the spanwise fluctuations, however, show the presence of elongated patches of instantaneous spanwise flow in the area $-60^\circ < \alpha < 60^\circ$, close to the stagnation line. The average distance in the spanwise direction between two adjacent elongated patches

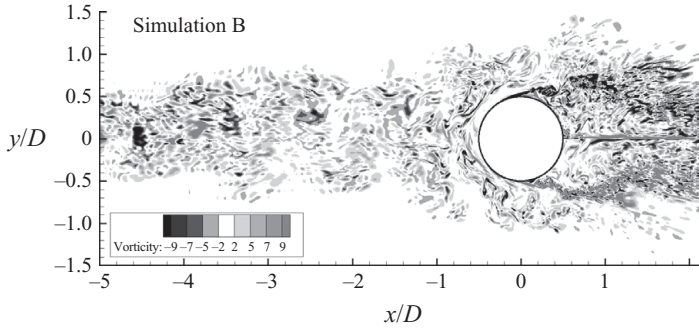


FIGURE 12. Snapshot showing contours of the instantaneous spanwise vorticity of simulation B at the midspan. The vorticity was made dimensionless using U/D .

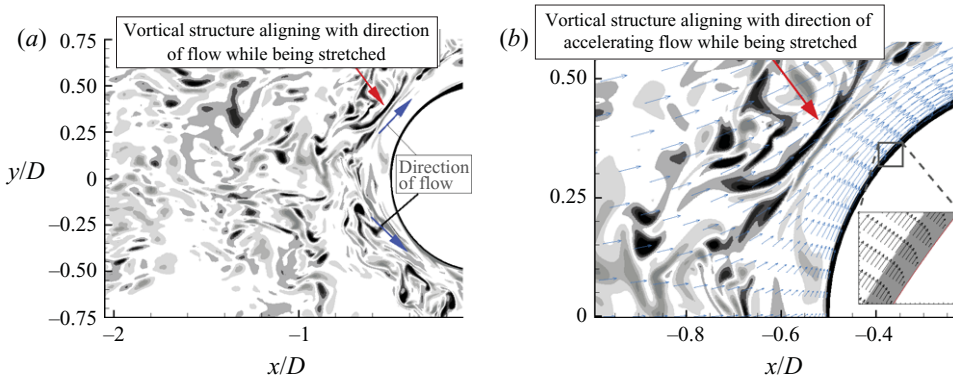


FIGURE 13. (Colour online) Snapshots showing contours of the instantaneous spanwise vorticity of simulation B near the upper part of the front of the cylinder. A more detailed view of the contours superposed with mean velocity field vectors is shown in (b). The inset shows a zoomed view of the boundary layer (with every third/fifth vector in the radial/circumferential direction).

of high w' values is approximately $0.25D$ and, as mentioned already, corresponds closely to the wavelength $\lambda = 0.286$ of the mode with wavenumber $k = 7$ from figure 6.

Figure 12 shows a snapshot of the spanwise vorticity at the midspan from simulation B. The snapshot clearly shows the vortical structures of the incoming wake that are present upstream of the cylinder. Close to the cylinder these structures become elongated and align with the direction of flow as they are stretched by the strongly accelerating flow immediately downstream of the stagnation line of the cylinder (see figure 13 for a more detailed view in which the boundary layer is identified by the thin black region adjacent to the cylinder). Close to the apex, the boundary layers can be seen to separate from the top and bottom of the cylinder (see also figure 9). Because of the presence of incoming fluctuations, the separated boundary layers can be seen to rapidly undergo transition. Without turbulence in the wake (simulation C), transition happens through a Kelvin–Helmholtz instability significantly farther downstream. As a result of the early transition in simulation B, intense vortical structures can be seen in the wake immediately behind the cylinder.

Figure 14(a) shows the vectors of the fluctuating velocity field at the midspan immediately in front of the cylinder. While many eddies can be observed up to a

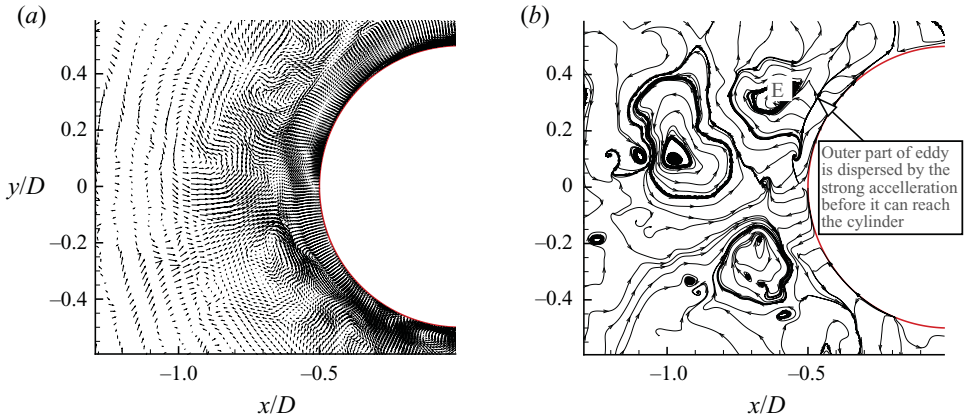


FIGURE 14. (Colour online) Snapshots showing the (a) vectors and (b) streaklines of the fluctuating velocity field $(u', v', 0)$ at the midspan of simulation B near the front of the cylinder.

distance of $0.05D$ – $0.15D$ of the cylinder's surface, the eddies appear to have difficulty in effectively penetrating this region, i.e. the immediate vicinity of the cylinder. The reason for this can be seen in figure 14(b), where the streakline plot clearly shows that the outer regions of the eddy labelled E are dispersed by the strongly accelerating mean flow before it can reach the immediate vicinity of the cylinder. This stretching of eddies by the accelerating flow (see also Xiong & Lele 2007) causes them to elongate and turn so that their axes align with the circumferential direction (see figure 22b). The behaviour of the eddies in the direct vicinity of the cylinder wall will be illustrated further by a series of snapshots of the velocity fluctuations in figure 20.

3.2. Heat transfer

As a dimensionless representation of the heat flux we use the local Nusselt number Nu , which, with the cylinder diameter D as the length scale, is defined by

$$Nu = \frac{q_w}{T_0 - \beta T_0} \frac{D}{k} = \frac{-1}{1 - \beta} \frac{\partial(\bar{T}/T_0)}{\partial(r/D)}, \quad (3.1)$$

where q_w is the heat flux at the wall; k is the thermal conductivity of the fluid; β is the ratio between the temperature of the outer flow and the temperature of the cylinder; and r is the radial (wall-normal) coordinate.

3.2.1. Time-averaged statistics

Profiles of the time-averaged temperature in the thermal boundary layer of simulations A, B and C at $\alpha = 0^\circ, 10^\circ, \dots, 50^\circ$ are shown in figure 15. Compared with simulation C, the mean temperature profile in simulation B is slightly fuller, and the edge of the thermal boundary layer is not well defined because of the diffusion of the temperature by the external fluctuations. Immediately downstream of the stagnation line, the gradients of the temperature profiles at the cylinder's surface in simulations A and B are very similar, while the gradient of the profile of simulation C is slightly smaller. The difference between simulations B and C reflects the increase in heat transfer due to the introduction of fluctuations into the boundary layer by the impinging wake. Accordingly, the Nusselt number, Nu , is also higher in

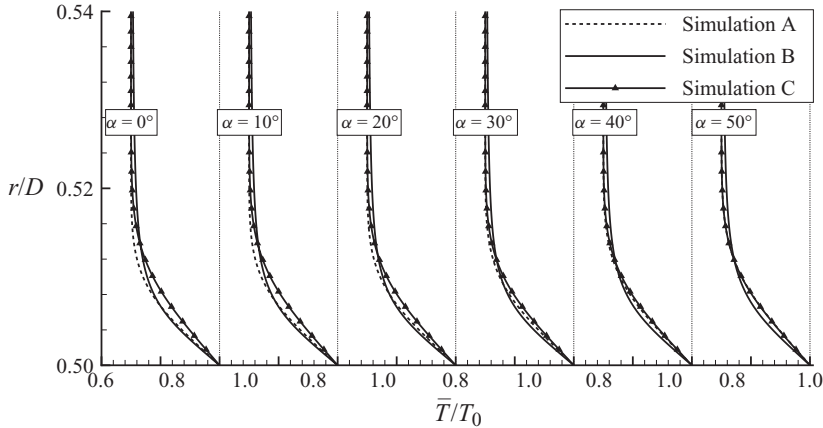


FIGURE 15. Simulations A, B and C: profiles of the time-averaged temperature in the thermal boundary layer at $\alpha = 0^\circ, 10^\circ, \dots, 50^\circ$.

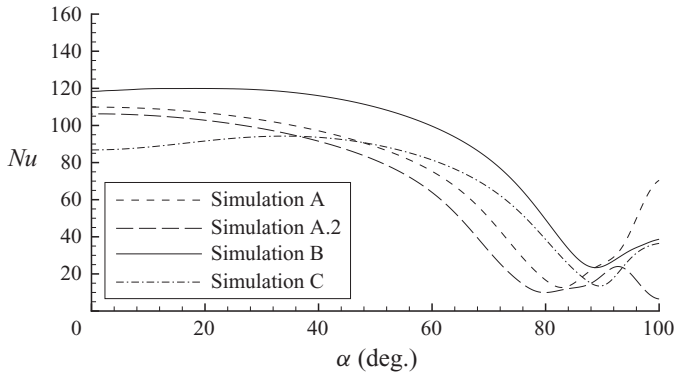


FIGURE 16. Simulations A, A.2, B and C: comparison of the time-averaged Nusselt number.

simulations A and B than in C as shown in figure 16. As was to be expected, there is no correlation between the skin friction coefficient (figure 9) and the Nusselt number in the stagnation region. In simulations A and A.2, Nu reaches a maximum at the stagnation line, while in simulations B and C, Nu shows a local minimum at $\alpha = 0^\circ$, which is a direct consequence of the velocity deficit in these two simulations. Because of the fluctuations present in the incoming wake of simulation B – compared with simulation C – the local minimum at $\alpha = 0^\circ$ is much less pronounced, and the heat transfer is found to be significantly increased in the entire stagnation region (at $\alpha = 0^\circ$ an increase in Nu by 37% is found). Compared with simulation A, the increase in Nu in simulation B is less pronounced, as the absence of a velocity deficit at the inflow in simulation A induces a stronger flow along the stagnation region of the cylinder, which results in a higher molecular heat transfer rate. The Nusselt number of simulation A.2 is slightly smaller than that of A, which indicates that the latter is not free of wall-parallel fluctuations which are likely to occur because of vortex shedding downstream, even though a splitter plate has been employed to limit these effects.

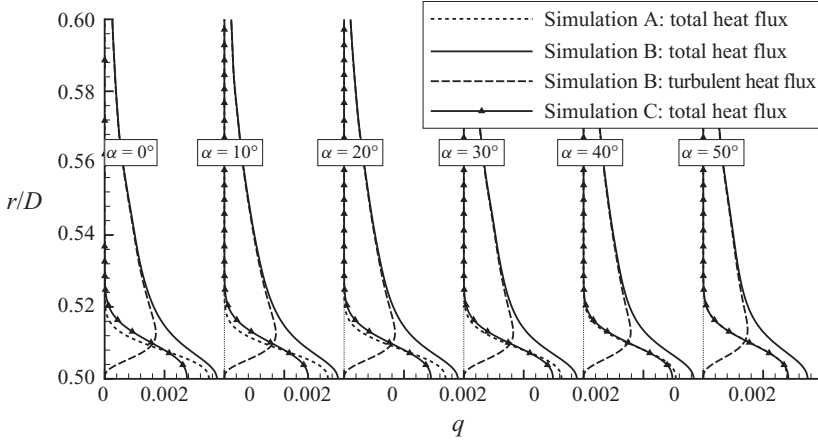


FIGURE 17. Simulations A, B and C: total and fluctuation-induced wall-normal heat flux.

Figure 17 shows the total wall-normal heat flux

$$q = \frac{1}{Re Pr} \left| \frac{\partial(\bar{T}/T_0)}{\partial(r/D)} \right| + \frac{|\overline{u'_r T'}|}{U_0 T_0} \quad (3.2)$$

from simulations A, B and C and the fluctuation-induced wall-normal heat flux $|\overline{u'_r T'}|/U_0 T_0$ of simulation B, where u'_r is the fluctuating velocity in the radial direction. Near the cylinder, radial fluctuations become restricted because of the presence of the wall, and the wall-normal fluctuation-induced heat transfer will reduce to zero. Hence, in this region the total heat flux in simulation B will be dominated by molecular heat transfer. Farther away from the cylinder, the wall-normal fluctuations can be seen to become responsible for a significant portion of the total wall-normal heat transfer, and above $r/D = 0.52$ the fluctuation-induced heat transfer completely dominates the heat transfer. Compared with the fluctuation-induced shear stress, $|\overline{u'_r T'}|/U_0 T_0$ is much more pronounced and remains non-negligible up to a distance of more than $0.1D$ away from the cylinder. In simulations A and C, where free-stream fluctuations are absent and $|\overline{u'_r T'}| = 0$, wall-normal heat transfer affects only the region up to approximately $0.02D$ away from the cylinder. Owing to the absence of a velocity deficit at the inflow plane, compared with simulation C, the wall-normal heat flux at the wall of simulation A is found to be higher.

The correlation of Dullenkopf & Mayle (1994) – based on the evaluation of heat transfer data from both cylinders in crossflow and turbine aerofoils – will now be introduced and tested. Involving the Reynolds number Re_D and the non-dimensional free-stream strain rate a_1 , these authors introduced a modified Nusselt number $Nu_a = Nu/\sqrt{a_1 Re_D}$ and a modified turbulence level $Tu_a = Tu_0\sqrt{Re_D/a_1}$ and correlated them by the relation

$$Nu_a Pr^{-0.37} = 0.571 + 0.0125 Tu_a \left\{ 1 + \frac{1.8}{[1 + (Tu_a/20)^3]} \right\}, \quad (3.3)$$

shown as a solid line in figure 18. For flow around a cylinder, the free-stream circumferential velocity near stagnation varies according to $U_c = a\alpha$, where a is the free-stream strain rate. Its non-dimensional value $a_1 = a D/U_0$, appearing in Nu_a and Tu_a , depends on the turbulence level, wind tunnel blockage and Reynolds number (see Kestin & Wood 1971). In the present work it is identified by the maximum value

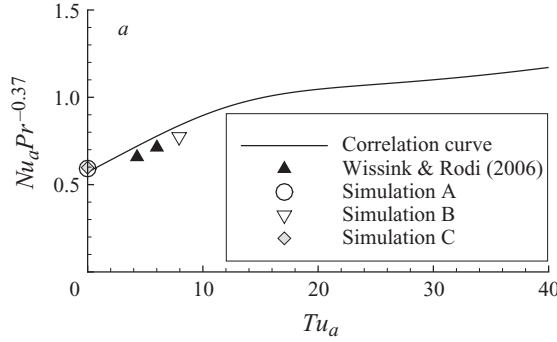


FIGURE 18. The correlation curve (3.3) of Dullenkopf & Mayle (1994) where $Nu_a Pr^{-0.37}$ is shown as a function of Tu_a . The symbols correspond to the results obtained in simulations A, B and C and in simulations II and III given in Wissink & Rodi (2006).

of $|\partial(U/U_0)/\partial(x/D)|$ along $y/D=0$ between the inflow and the stagnation point, which occurs very close to the wall. The values of a_1 determined for the various simulations are $a_1=3.38$ for A, $a_1=2.38$ for B and $a_1=2.06$ for C. The value of the turbulence level Tu_0 is taken as the minimum value of Tu along $y/D=0$. For simulation B the minimum, $Tu_0=0.1057$ (not a percentage), is found at the location indicated by the arrow in figure 5(b). In figure 18 the time-averaged (Tu_a, Nu_a) results from simulations A, B and C are compared with the correlation curve. The two black triangles identify the results obtained at the stagnation point of a model turbine blade in the DNSs labelled II and III in Wissink & Rodi (2006). The origin of the correlation curve, i.e. the situation without oncoming free-stream turbulence, is predicted very well by the two simulations A and C with fluctuation-free inflow. The simulations with incoming wakes (triangles in figure 18) do predict the increase in heat transfer with increasing free-stream turbulence level but fall a little below the correlation curve.

In order to account also for the effect of the integral turbulence length scale Λ on the augmentation of stagnation heat transfer, Dullenkopf & Mayle (1995) introduced a dimensionless integral length scale $L_a = (\Lambda/D)\sqrt{a_1 Re_D}$ and a turbulence parameter

$$Tu_\lambda = \frac{Tu_a \sqrt{L_a}}{[1 + 0.004L_a^2]^{5/12}} \quad (3.4)$$

and subsequently replaced (3.3) by the correlation

$$Nu_a Pr^{-0.37} = 0.571 + 0.01 Tu_\lambda, \quad (3.5)$$

with Tu_a , a_1 and Nu_a calculated as above. The integral length scale Λ is taken as Λ_u shown in figure 6(a) and is determined at the same location as Tu_0 . In simulation B, the integral length scale at $x/D=-0.78$ is $\Lambda_u=0.0526D$ so that the correlation (3.5) of Dullenkopf & Mayle (1995) predicts a value of 0.783, while the DNS predicts a value of $Nu_a Pr^{-0.37}=0.758$, which is a slight underestimation by approximately 3.2%.

Ames (1997) and Ames *et al.* (2003) correlated the effect of turbulence on stagnation heat transfer by the relation

$$Nu/Nu_0 = 1 + 0.04 Tu_0 Re_D^{5/12} (L_u/D)^{-1/3}, \quad (3.6)$$

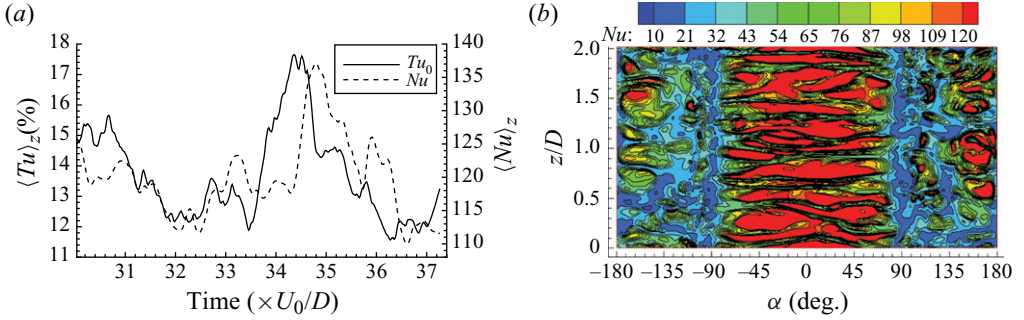


FIGURE 19. Simulation B: (a) joint variation with time of the spanwise-averaged turbulence level $\langle Tu \rangle_z$ (at $x/D = -0.78$) and Nusselt number $\langle Nu \rangle_z$ (at stagnation); (b) snapshot showing contours of the instantaneous Nusselt number at the same time as the snapshots of the streamwise and spanwise fluctuating velocity presented in figure 11.

where Nu_0 is the stagnation heat transfer in the baseline situation without free-stream turbulence, while the parameter $Tu_0 Re_D^{5/12} (L_u/D)^{-1/3}$ was obtained by Ames & Moffat (1990) with the aid of rapid distortion theory; L_u is the energy length scale whose distribution ahead of the cylinder is given in figure 6(a). The value taken at $x/D = -0.78$ is $L_u = 0.65D$. With Tu_0 as before, (3.6) predicts a value of $Nu/Nu_0 = 1.25$. Taking simulation C as the baseline simulation yielding Nu_0 , from simulation B we obtain $Nu/Nu_0 = 1.36$. The match with the correlation is less satisfactory but is still reasonable in view of the large uncertainties in defining and determining the turbulence-level and length-scale parameters.

3.2.2. Instantaneous temperature and heat transfer

As opposed to grid turbulence, the presence of a near-wake causes a significant variation with time in the turbulence level of the incoming flow and, as a result, also of the Nusselt number at stagnation. Figure 19(a) illustrates the joint variation of the spanwise-averaged Nusselt number $\langle Nu \rangle_z$ at stagnation and the spanwise-averaged turbulence level $\langle Tu \rangle_z$ at $x/D = -0.78$ – which is defined similarly to Tu in (2.1) but with time averaging (denoted by the bar) replaced by spanwise averaging $\langle \cdot \rangle_z$. There is a close correspondence between the two signals but also a time lag due to the time it takes the fluctuations at $x/D = -0.78$ to reach the stagnation point. Accounting for this time lag, the correlation between $\langle Nu \rangle_z$ and $\langle Tu \rangle_z$ is about 0.80, indicating that the variation in heat transfer directly follows the fluctuations.

Figure 20 shows how individual eddies impinging on the cylinder affect heat transfer. The figure displays a series of snapshots with vectors of the fluctuating velocity field at the midspan adjacent to the cylinder wall. The corresponding instantaneous Nusselt number distribution along the cylinder's circumference is shown at the right. At time t_1 , Nu is found to be almost constant, as no strong eddies are present close to the cylinder. When the counterclockwise-rotating eddy identified by V approaches the cylinder (between t_1 and t_2), underneath its centre cold fluid from the free stream is transported towards the heated cylinder, causing the local Nusselt number to increase. The vortex is elongated by the mean acceleration as it is transported upwards along the cylinder's surface between t_2 and t_3 , and the Nusselt number increases further in the downwash region. Between t_4 and t_5 a clockwise-rotating eddy identified by the label C can be seen to move downwards as it approaches the cylinder. At t_5 the strong disturbance associated with the eddy completely destroys the local boundary layer. Again in the downwash region of the eddy (now the upper side), cold fluid is

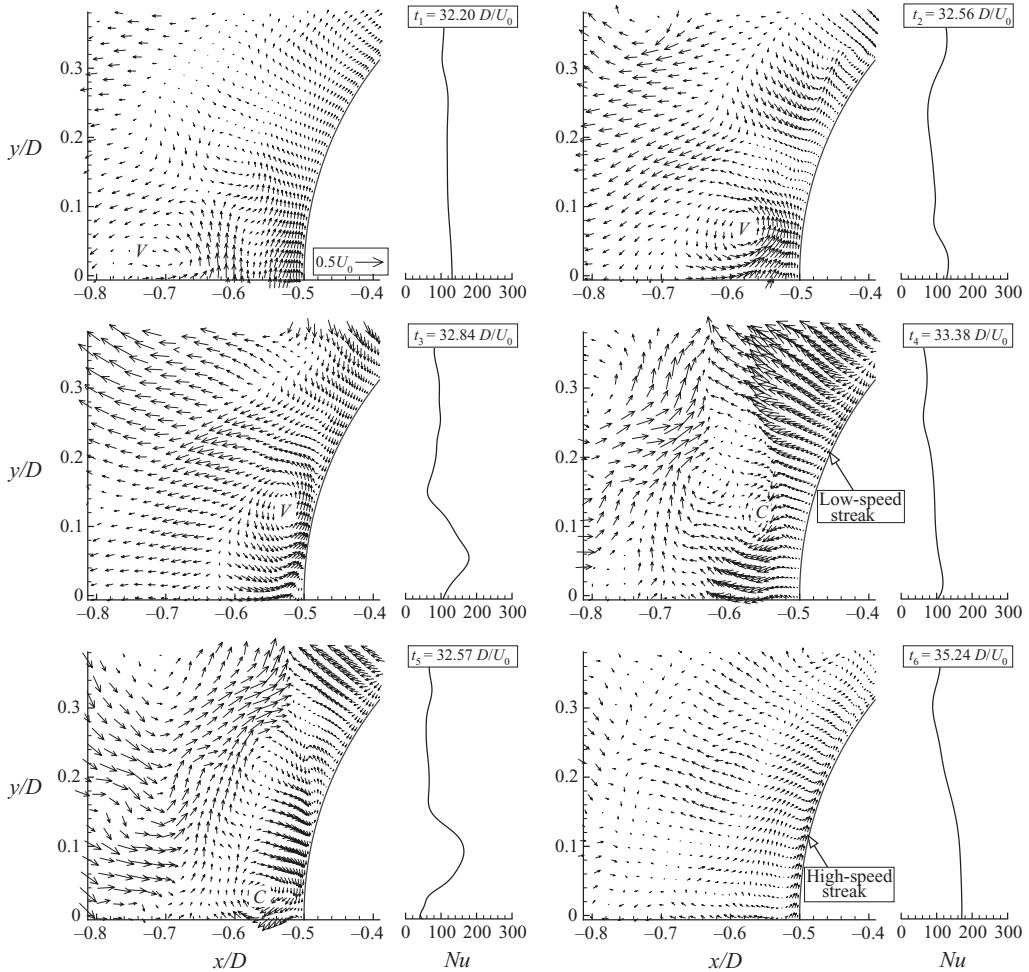


FIGURE 20. Series of snapshots of the fluctuating velocity vectors in the plane at the midspan (zoomed view), showing every seventh vector in both the circumferential and radial directions. The panels on the right show the instantaneous Nusselt number.

transported to the heated cylinder, resulting in a local increase in Nu , while below the eddy hot fluid is transported away from the cylinder, which causes a local minimum in Nu . At t_4 and t_6 low- and high-speed streaks can be observed, respectively. However, the streamwise fluctuations in figure 11(a) indicate that these streaks are fairly weak in the stagnation region. Hence, unlike in the case of heat transfer from a heated flat plate subjected to an accelerating turbulent free stream studied by Wissink & Rodi (2009), these streaks do not seem to be responsible for the increase in heat transfer in the stagnation region of the cylinder. Instead, a correlation is found between high values of the instantaneous Nusselt number, shown in figure 19(b), and high/low values of the fluctuating spanwise velocity (see figure 11b), and it will now be shown that the increase in heat transfer observed in simulation B is mainly caused by near-wall streamwise vortices originating from the stretching of free-stream vorticity by the accelerating flow near the stagnation region.

Figure 21 shows snapshots at $t = 29.99 D/U_0$ of the vector field of the instantaneous fluctuating velocity $\|\mathbf{u}' = \mathbf{u} - \langle \mathbf{u} \rangle\|$ and contours of the instantaneous temperature field

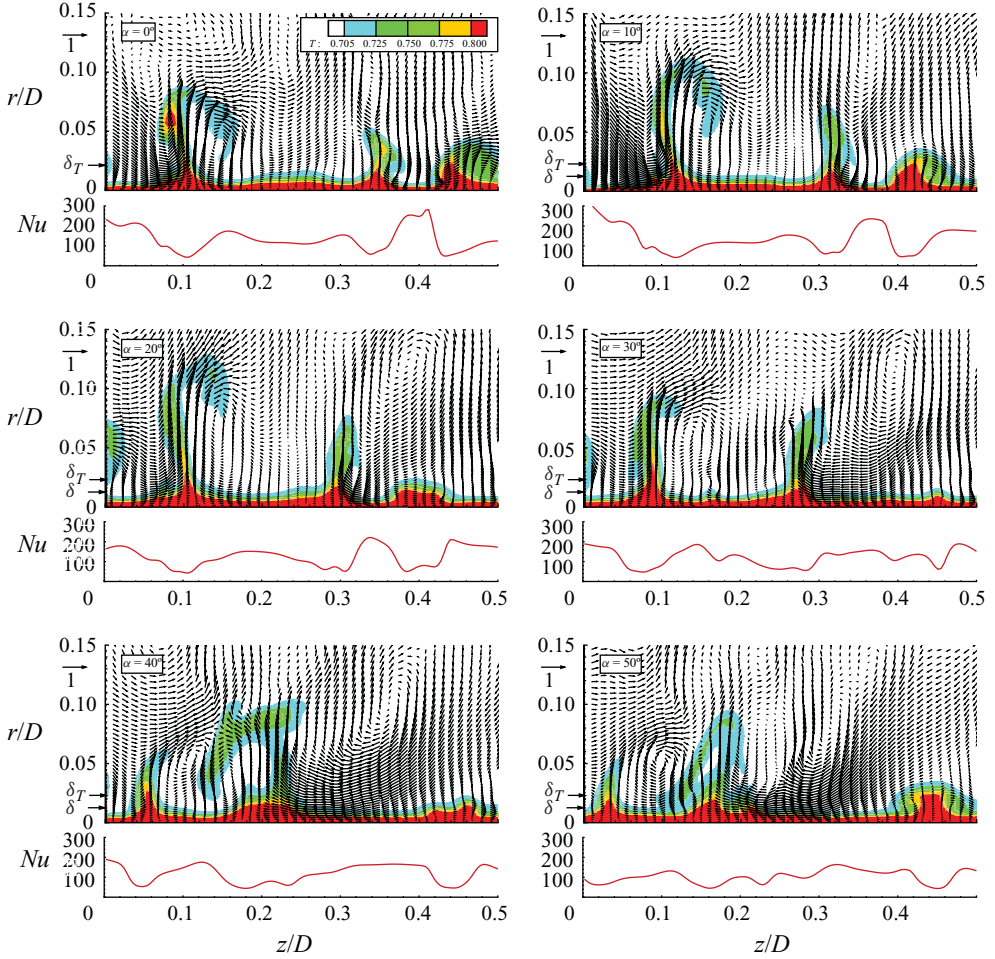


FIGURE 21. Simulation B: the upper panels in all sub-parts show the temperature contours T/T_0 and the vector field of the fluctuating velocity in cross-sections of the cylinder boundary layer at $\alpha = 0^\circ, 10^\circ, 20^\circ, \dots, 50^\circ$ and $t = 29.99 D/U_0$. The vector field shows vectors in every third point. The thickness of the viscous and thermal boundary layers are identified by δ (except at $\alpha = 0^\circ$) and δ_T , respectively. The lower panels of all sub-parts show the instantaneous Nusselt numbers.

T/T_0 in the vicinity of the cylinder in the cross-sections at $\alpha = 0^\circ, 10^\circ, 20^\circ, 30^\circ, 40^\circ, 50^\circ$ from simulation B. The thickness of the viscous and thermal boundary layers in these cross-sections is identified by δ and δ_T , respectively, where δ is the distance from the cylinder of the location where the circumferential velocity u_c first reaches 99% of its maximum value and δ_T is the distance from the cylinder of the location where the temperature reaches a value of $T = 0.715T_0$. The sequence of cross-sections gives evidence of the presence of thin, elongated rotating structures whose axes are aligned with the direction of flow. Even though there is no time-averaged circumferential flow at the stagnation line, figure 22(b) illustrates that the elongated structures span the entire stagnation region. For instance, one of these structures (see figure 21) is located in the cross-section at $\alpha = 0^\circ$ with coordinates $z/D \approx 0.15$ and $r/D \approx 0.04$. The same structure can be easily identified in the downstream cross-sections at $\alpha = 10^\circ, 20^\circ$ and

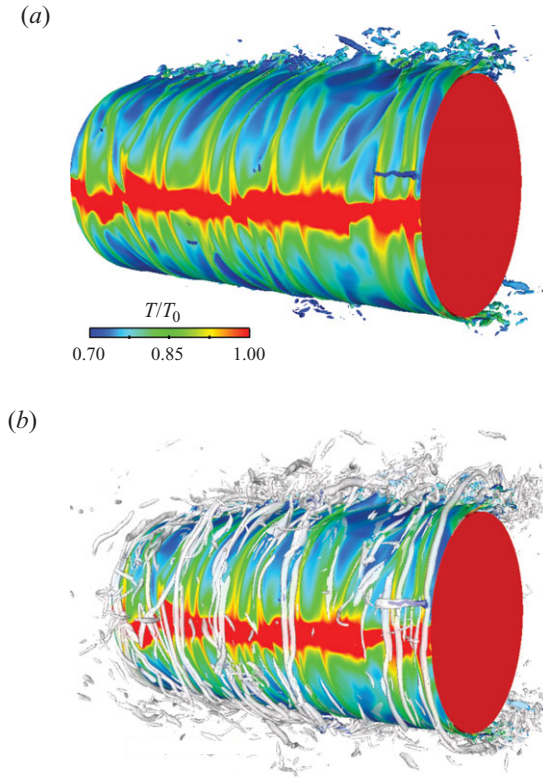


FIGURE 22. Simulation B. (a) Snapshots showing the boundary layer developing in the stagnation region of the cylinder identified by the isosurfaces of the instantaneous spanwise vorticity at $\omega_z = \pm 40$ coloured with the temperature. (b) As in (a), superposed with translucent elongated structures that evolved from vortical structures from the incoming wake and are made visible using the λ_2 -criterion of Jeong & Hussain (1995)

30° , and even farther downstream it is still likely to be present. As such a rotating structure impinges, at one side of it cold fluid is transported towards the heated cylinder, and on its other side hot fluid is peeled away from the wall of the cylinder towards the free stream. The contours of the temperature clearly show that hot fluid is transported upwards over distances of more than $0.1D$ into the free stream. This is reflected in the normal heat flux profiles in figure 17, which show a significant turbulent transport of heat up to a distance of $0.1D$ away from the cylinder in simulation B. The small graphs at the bottom of each panel show the distribution of the instantaneous Nusselt number in the spanwise direction. It can be seen that each time hot fluid from the surface of the cylinder is swept up into the cold free stream the instantaneous Nusselt number shows a minimum. The maxima in the instantaneous Nusselt number are reached in between these events where cool fluid from the free stream is transported towards the heated surface of the cylinder, thereby increasing the temperature gradient at the wall, and hence, because of increased molecular heat, transfer the Nusselt number. The same mechanism has already been found in figure 20 for eddies with the spanwise vorticity impinging on the cylinder.

The snapshots in figure 22 show the evolution of the boundary layers downstream of the stagnation line along both the upper and lower parts of the cylinder. Additionally, in figure 22(b) the circumferential vortical structures near the cylinder have been made

visible using the λ_2 -criterion. As predicted by Hunt (1973) and Xiong & Lele (2007), near the cylinder the accelerating flow is observed to severely stretch the vortical structures of the wake into thin, elongated tubes that are aligned with the direction of flow and completely wrap around the stagnation region of the cylinder (see figure 22*b*). The spatial distribution of these vortex tubes corresponds to the disturbance pattern that is found on the cylinder's boundary layer, as illustrated in figure 22(*a*). This confirms the earlier observation, made in figure 21, where the rotating structures that are observed in cross-sections at various locations in the stagnation region of the cylinder exactly correspond to the vortex tubes shown in figure 22(*b*). Also, the average distance between two adjacent vortex tubes is approximately $0.25D$, which almost equals the peak observed at $\lambda = 0.286D$ in the spanwise spectral distribution of the w -velocity in figure 6, corresponding to the approximate size of the vortices with streamwise rotation in the incoming wake.

4. Discussion and conclusions

DNSs of flow around and heat transfer from the stagnation area of a circular cylinder with and without the presence of an impinging wake have been performed. The choice of the flow situation was inspired by the experimental set-up used by Magari & LaGraff (1994). The effect of the wake of a small upstream cylinder in this experiment was modelled by wake data that were gathered in a separate precursor simulation presented in Wissink & Rodi (2008). These data were subsequently introduced at the inflow plane. Compared with the experiments, the (virtual) distance between the wake-generating cylinder and the main cylinder was significantly larger, as the inflow plane needed to be at least $5D$ upstream of the cylinder in order to avoid the prescribed inflow conditions to artificially limit the upstream effects of stagnation. Also, a splitter plate was applied at the back of the cylinder to counteract the formation of a vortex street.

Apart from simulation B with the incoming realistic wake, three further (baseline) simulations were performed. Simulation A was three-dimensional, and the wake was replaced by a uniform flow at the inflow plane. Simulation A.2 was two-dimensional, restricted to half the flow domain above the symmetry plane, and – like simulation A – had a uniform inflow. In simulation C, finally, turbulence was removed from the wake data at the inflow plane, keeping the same mean velocity deficit and the same half-width as in simulation B.

The presence of the realistic wake in simulation B was found to lead to an increase in the Nusselt number at the stagnation line of 37% when compared with simulation C, while compared with simulation A this increase was found to be less significant.

The incoming disturbances in simulation B were found not to trigger boundary-layer transition in the stagnation region, as evidenced by the close agreement obtained in the circumferential velocity profiles of simulations B and C at various stations. Also the large values reached by the acceleration parameter K – which were well in excess of the value of $K = 2.5 \times 10^{-6}$ that would be needed to relaminarise a turbulent boundary layer – indicate that boundary-layer transition did not happen in any of the simulations. However, instantaneously and locally the impinging eddies were found to strongly disturb (and sometimes even destroy) the laminar boundary layer.

While in simulation B the contribution of the turbulent shear stress to the total shear stress is relatively small and is only noticeable fairly close to the cylinder, the contribution of the turbulent heat flux to the total wall-normal heat flux is significant and reaches quite far (up to about $0.1D$) into the free stream. Only very close to

the cylinder does the presence of the wall damp normal fluctuations, which forces the turbulent heat flux to become zero. This significant difference in importance between the turbulent shear stress and the turbulent heat flux – as compared with their contribution to the total shear stress and heat flux, respectively – is typical for the promotion of laminar heat transfer by external fluctuations.

Overall good agreement was achieved between the Nusselt number at the stagnation line obtained in the numerical simulations with the correlations of Dullenkopf & Mayle, both the one with (1995) and the one without (1994) involving the integral length scale of the oncoming turbulence. For the baseline simulation with laminar inflow, there was insignificant difference between the simulation and the correlation value of Nu , while for the simulation with incoming turbulent wake the DNS yielded a slightly lower Nu than the correlations. Also, compared with the correlation of Ames (1997) involving the ‘energy’ length scale L_u , the same order of heat transfer was obtained by the DNS, but the quantitative difference was larger. This points to considerable uncertainties in the specification of the turbulence-level and length-scale parameters.

In the vicinity of the stagnation line the increase in laminar heat transfer observed in simulation B was found to be caused by impinging, elongated vortical structures that were approximately aligned with the circumferential direction. These structures – which were found earlier in the numerical simulations of Xiong & Lele (2007) and have already been derived from the theories of Hunt (1973) and Xiong & Lele (2004) – were observed to be formed when the vortical structures of the incoming wake were stretched by the strongly accelerating, almost wall-parallel flow in the stagnation region of the cylinder. As a result of this stretching, the vortical structures became long and thin, and their axes tended to align with the direction of flow around the cylinder except at the stagnation line. The distance between the individual structures was found to be closely related to the diameter of the vortices with streamwise rotation present in the incoming wake. The elongated vortices promote heat transfer by transporting cool fluid from the outer flow towards the heated cylinder on their downward-moving side and by transporting hot fluid away from the cylinder towards the free stream on their upward-moving side. By itself, the transport of hot fluid from the cylinder’s surface towards the free stream leads to a local decrease in the Nusselt number. However, this peeling of hot fluid away from the wall is very localised. The transport of cool fluid towards the cylinder – on the other hand – takes place in much broader regions, thereby causing an overall increase in Nu .

The authors would like to thank the German Research Foundation (DFG) for funding this research through project Ro558/30-1 and the steering committee of the Super Computing Facilities in Bavaria (HLRB) for granting computing time on the SGI Altix 4700 at the Leibniz Computing Centre (LRZ) in Munich.

REFERENCES

- AMES, F. E. 1997 The influence of large-scale high-intensity turbulence on vane heat transfer. *ASME J. Turbomach.* **119**, 23–30.
- AMES, F. E. & MOFFAT, R. J. 1990 Heat transfer with high-intensity large-scale turbulence: the flat plate turbulent boundary layer and the cylindrical stagnation point. *Rep. HMT-44*. Thermosciences Division of Mechanical Engineering, Stanford University.
- AMES, F. E., WANG, C. & BARBOT, P. A. 2003 Measurement and prediction of the influence of catalytic and dry low NO_x combustor turbulence on vane surface heat transfer. *ASME J. Turbomach.* **125**, 221–231.

- BHASKARAN, R. & LELE, S. 2010 Large eddy simulation of free-stream turbulence effects on heat transfer to a high pressure turbine cascade. *J. Turbul.* **11**, 1–15.
- BREUER, M. & RODI, W. 1996 Large eddy simulation for complex turbulent flows of practical interest. In *Flow Simulation with High Performance Computers II: Notes on Numerical Fluid Mechanics* (ed. E. H. Hirschel), vol. 52, pp. 258–274. Vieweg.
- BRITTER, R. E., HUNT, J. C. R. & MUMFORD, J. C. 1979 The distortion of turbulence by a circular cylinder. *J. Fluid. Mech.* **92**, 269–301.
- DULLENKOPF, K. & MAYLE, R. E. 1994 The effects of incident turbulence and moving wakes on laminar heat transfer in gas turbines. *ASME J. Turbomach.* **116**, 23–28.
- DULLENKOPF, K. & MAYLE, R. E. 1995 An account of free-stream-turbulence length scale on laminar heat transfer. *ASME J. Turbomach.* **117**, 401–406.
- DULLENKOPF, K., SCHULZ, A. & WITTIG, S. 1991 The effect of incident wake conditions on the mean heat transfer of an airfoil. *ASME J. Turbomach.* **113**, 412–418.
- VAN FOSSEN, G. J., SIMONEAU, R. J. & CHING, C. Y. 1995 Influence of turbulence parameters, Reynolds number and body shape on stagnation point heat transfer. *J. Heat Transfer* **125**, 221–231.
- HERNON, D., WALSH, E. J. & MCELIGOT, D. M. 2007 Experimental investigation into the routes to bypass transition and the shear-sheltering phenomenon. *J. Fluid. Mech.* **591**, 461–479.
- HUNT, J. C. R. 1973 A theory of flow round two-dimensional bluff bodies. *J. Fluid. Mech.* **61**, 625–706.
- JEONG, J. & HUSSAIN, F. 1995 On the identification of a vortex. *J. Fluid. Mech.* **285**, 69–94.
- JONES, W. P. & LAUNDER, B. E. 1973 The calculation of low Reynolds number phenomena with a two-equation model of turbulence. *Intl J. Heat Mass Transfer* **16**, 1119–1130.
- JUNKHAN, G. H. & SEROVY, G. K. 1967 Effects of free-stream turbulence and pressure-gradient on flat plate boundary layer velocity profiles and on heat transfer. *ASME J. Heat Transfer* **89**, 169–176.
- KESTIN, J., MAEDER, P. F. & WANG, H. E. 1961 Influence of turbulence on heat transfer of heat from plates with and without a pressure gradient. *Intl J. Heat Mass Transfer* **3**, 133–154.
- KESTIN, J. & WOOD, R. T. 1971 The influence of turbulence on mass transfer from cylinders. *ASME J. Heat Transfer C* **93**, 321–327.
- LIU, X. & RODI, W. 1994a Velocity measurements in wake-induced unsteady flow in a linear turbine cascade. *Exp. Fluids* **17**, 45–58.
- LIU, X. & RODI, W. 1994b Surface pressure and heat transfer measurements in a turbine cascade with unsteady oncoming wakes. *Exp. Fluids* **17**, 171–178.
- LOWERY, G. W. & VACHON, R. L. 1975 The effect of turbulence on heat transfer from heated cylinders. *Intl J. Heat Mass Transfer* **18**, 1229–1242.
- MAGARI, P. J. & LAGRAFF, L. E. 1994 Wake-induced unsteady stagnation-region heat transfer measurements. *ASME J. Turbomach.* **116**, 29–38.
- MAYLE, R. E., DULLENKOPF, K. & SCHULZ, A. 1998 The turbulence that matters *ASME J. Turbomach.* **120**, 402–409.
- PAXSON, D. E. & MAYLE, R. E. 1991 Laminar boundary layer interaction with an unsteady passing wake. *ASME J. Turbomach.* **113**, 419–427.
- RHIE, C. M. & CHOW, W. L. 1983 Numerical study of the turbulent flow past an airfoil with trailing edge separation. *AIAA J.* **21**, 1525–1532.
- SCHULZ, A. 1986 Zum Einfluß höher Einstromturbulenz, intensiver Kühlung und einer Nachlaufströmung auf den äußeren Wärmeübergang einer konvektiv gekühlten Gasturbinenschaufel. PhD thesis, University of Karlsruhe, Karlsruhe, Germany.
- SIKMANOVIC, S., OKA, S. & KONCAR-DJURDJEVIC, S. 1974 Influence of the structure of turbulent flow on heat transfer from a single cylinder in a cross flow. In *Proceedings of the 5th International Heat Transfer Conference*, Tokyo, vol. 2, pp. 320–324. A.I.Ch.E.
- VAN DRESAR, N. T. 1987 The effect of incident wake-flow on blunt body transfer rates. PhD thesis, Rensselaer Polytechnic Institute, Troy, NY.
- WISSINK, J. G. & RODI, W. 2006 Direct numerical simulation of flow and heat transfer in a turbine cascade with incoming wakes. *J. Fluid Mech.* **569**, 209–247.
- WISSINK, J. G. & RODI, W. 2008 Numerical study of the near wake of a circular cylinder. *Intl J. Heat Fluid Flow* **29**, 1060–1070.

- WISSINK, J. G. & RODI, W. 2009 DNS of heat transfer in transitional, accelerated boundary layer flow over a flat plate affected by free-stream fluctuations. *Intl J. Heat Fluid Flow* **30**, 930–938.
- XIONG, Z. & LELE, S. K. 2004 Distortion of upstream disturbances in a Hiemenz boundary layer. *J. Fluid Mech.* **519**, 201–232.
- XIONG, Z. & LELE, S. K. 2007 Stagnation point flow under free-stream turbulence. *J. Fluid Mech.* **590**, 1–33.
- YARDI, N. R. & SUKHATME, S. P. 1978 Effect of turbulence intensity and integral length scale of a turbulent free stream on forced convection heat transfer from a circular cylinder in cross flow. In *Proceedings of the 6th International Heat Transfer Conference*, Toronto, Canada, vol. 5, FC(b)-29, pp. 347–352. Hemisphere Press, Washington D.C.
- ZAKI, T. A., WISSINK, J. G., DURBIN, P. A. & RODI, W. 2009 Direct computations of boundary layers distorted by migrating wakes in a linear compressor cascade *Flow Turbul. Combust.* **83**, 930–938.